RF Performance and Avalanche Breakdown Analysis of InN Tunnel FETs

Krishnendu Ghosh, *Student Member, IEEE*, and Uttam Singisetti, *Member, IEEE*

***Abstract*— This paper reports radio frequency (RF) performance and channel breakdown analysis in an n-type tunneling field-effect transistor based on InN. The tunneling current is evaluated from the fundamental principles of quantum mechanical tunneling. We investigate the RF performance of the device. High transconductance of 2.18 mS/μm and current gain cutoff frequency of 460 GHz makes the device suitable for terahertz applications. A significant reduction in gate-to-drain capacitance is observed under a relatively higher drain bias (V_{ds} = 1 V). Impact ionization coefficient in the channel is evaluated quantitatively considering semiclassical carrier transport and avalanche breakdown is found to be unlikely at V_{ds} = 1.0 V.**

***Index Terms*— Avalanche mechanism, gate-to-drain capacitance, high power terahertz application, InN, ionization coefficient, tunnel field-effect transistor (TFET), Wolff's theory.**

I. Introduction

TUNNEL field-effect transistors (TFETs) have achieved a lot of attention in recent years as post-CMOS logic devices due to their steep subthreshold slope (SS) (SS < 60 mV/decade) [1], [2]. III–V semiconductors are attractive as TFET channel materials for low power applications due to their low tunnel effective mass and small bandgap that leads to high tunnel transmission probability. Although TFETs are extensively investigated for logic application, there has only been a few reports on their high speed radio frequency (RF) performance [3]–[7]. Low transconductance (g_m) and high gate to drain feedback capacitance (C_{gd}) are identified as the challenges to implement TFETs in high frequency applications [4]–[6]. Double-gate TFETs with high-k dielectric [7] and gate-all-around TFETs [3] have also been explored to improve the high frequency performance with limited success. Recently, InAs vertical TFETs [8], [9] with an n+ pocket in source have been demonstrated to boost up the on current (I_{ON}) but high C_{gd} is still an area of concern for TFETs as far as the RF performance is concerned. There has been a recent experimental report of an III–V TFET with an extrinsic current gain cutoff frequency of 19 GHz [10]. Here, we report on the RF performance of InN TFET evaluated using SILVACO ATLAS [11] simulations and show that the high C_{gd} could be overcome by operating at a relatively higher V_{ds} without the risk of avalanche breakdown in the channel region.

InN is an attractive TFET channel material due to its small electron effective mass (0.07 m_0) and moderately high bandgap (0.7 eV). The potential of InN for high speed electronic devices has long been recognized [12]–[14]. However, there have been a few experimental demonstrations [15] due to high unintentional doping [16] and large surface band bending in InN [17]. Although p-type doping have been experimentally demonstrated in InN [18], high degenerate p-type doping has also been a challenge in InN as is the case for all III-Ns. Higher p-type doping could potentially be achieved using polarization doping [19]. Tunnel junctions [20] also provide a promising alternative to p-type contacts. Recently, there have also been reports of unpinned surfaces on N-polar [21] and semipolar surfaces [22]. The N-polar and semipolar technologies are promising and they could potentially provide the pathway for experimental InN devices.

In this paper, we focus on the fundamental limits of InN TFET devices arising from the intrinsic materials properties by numerical simulation and semianalytical calculations. We analyze a single gate InN TFET, which shows an excellent RF performance with a peak current gain cutoff frequency (f_t) of around 0.5 THz. The proposed device is simulated in SILVACO ATLAS taking nonlocal band-to-band tunneling model into account. Semianalytical tunneling current calculation is carried out to calibrate the simulator.

We analyze the high frequency performance of the device. As reported in the literature, high C_{gd} in TFETs is a bottleneck to the RF operation of the devices. Usually, TFETs are operated at lower voltages (V_{ds} < 0.3 V) for logic applications. This paper shows that a higher drain voltages (V_{ds} = 1 V) could be a solution to reduce C_{gd} and hence to obtain an improved RF performance. However, use of higher V_{ds} makes it essential to explore the avalanche breakdown mechanism in the device. Avalanche breakdown in the proposed InN device is explored quantitatively. The electron impact ionization coefficient was calculated from Boltzmann transport equation (BTE) considering polar optical phonon (POP) scattering. The calculations show that InN TFETs can be operated at V_{ds} = 1.0 V without channel avalanche breakdown. The symbols used in this paper are shown in Table I.

II. TFET Tunneling Current

In this section, we first evaluate the current drive capability of InN TFETs. We consider a 50-nm gate length device,

Manuscript received January 31, 2014; revised July 14, 2014; accepted July 29, 2014. Date of publication August 14, 2014; date of current version September 18, 2014. This work was supported by the Department of Electrical Engineering, University at Buffalo, The State University of New York, Buffalo, NY, USA. The review of this paper was arranged by Editor D. Esseni.

The authors are with the University at Buffalo, The State University of New York, Buffalo, NY 14260 USA (e-mail: kghosh3@buffalo.edu; uttamsin@buffalo.edu).

Color versions of one or more of the figures in this paper are available online at http://ieeexplore.ieee.org.

Digital Object Identifier 10.1109/TED.2014.2344914

TABLE I
LIST OF SYMBOLS USED IN THIS PAPER

Symbols used for tunneling action analysis		Symbols used for avalanche action analysis	
Symbol	Quantity	Symbol	Quantity
F	Electric Field	F_z	Electric Field in transport direction
k (with suitable subscripts)	Wave vector (in different directions)	E_R	Phonon energy
E (withsuitable subscripts)	Energy(in different directions)	w	Depletion width
t_{HfO_2}	Oxide thickness	λ	Electron mean free path
t_{InN}	Transistor body thickness	α	Ionization coefficient
ϵ_{InN}	Dielectric constant of InN		
ϵ_{ox}	Dielectric constant of oxide		
Λ	Screening length		
J_{ds}	Current density		

TABLE II
DESIGN AND MATERIALS PARAMETERS FOR THE DEVICE

Oxide		InN	
Permittivity	15.6	Bandgap	0.7 eV
Thickness	3nm	Electron tunnel mass	$0.07m_0$
Bandgap	6 eV	Hole tunnel mass	$0.27m_0$
Gate Metal		e saturation velocity	3×10^7 cm/s
Work function	4.3 eV	Low field e mobility	$1500cm^2/Vs$
Doping Profile		Body Thickness	10nm
Source	10^{20} cm^{-3} (p)	Gate length	50nm
Drain	10^{20} cm^{-3} (n)	Permittivity	15.3
Channel	10^{17} cm^{-3} (n)	Electron Affinity	5.34 eV

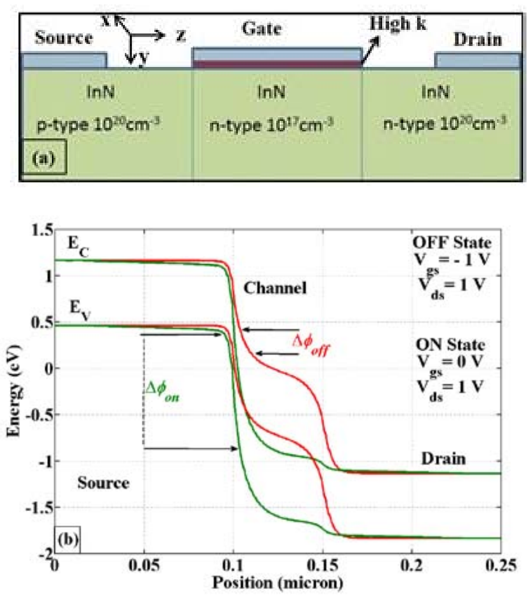

Fig. 1. (a) Structure of the simulated device, buried oxide substrate not shown. (b) Simulated energy band diagram in (red curves) OFF state ($V_{gs} = -1$) and (green curves) ON state ($V_{gs} = 0$) for V_{ds} of 1 V.

as shown in Fig. 1(a). The device and materials parameters used in the simulations are shown in Table II. Fig. 1(b) shows the simulated energy band diagrams in the ON and OFF states of the device, $\Delta\Phi_{ON}$ and $\Delta\Phi_{OFF}$ are the tunneling energy windows for electrons in the source in the ON and OFF states, respectively. The tunnel energy window is taken to be the difference between in the valence band (VB) maxima in the source and the conduction band minima in the channel. The current in the device is controlled by changing the tunnel energy window ($\Delta\Phi$) by the gate bias. Next, we calculate the tunneling probability in the structure to evaluate the current.

A. Tunneling Current

Fig. 1(b) shows the simulated band diagram of the device in the ON and OFF states. Starting from the simulated band diagram at a particular bias point [Fig. 1(b)], we calculate the tunneling probability under Wentzel-Kramer-Brillouin formalism. We consider elastic tunneling mechanism, assuming the longitudinal electric field (F_z) to be constant across the tunneling path. While the ATLAS simulator uses a nonlocal tunneling model; here, we find that semianalytical calculation with a suitable choice of constant electric field can closely match the simulated tunneling current providing insight into the device operation.

The conservation of transverse angular momentum (k_x and k_y) and transverse energy ($E_\perp$) in the tunneling process simplifies the problem to an 1-D tunneling problem with a modified effective bandgap (E_g^*) for tunneling. In a purely 1-D tunneling case, where the electrons do not have any transverse momentum ($E_\perp = 0$), the barrier seen by a tunneling electron at the classical turning point [Fig. 2(a)] on the VB side is $E_g + (\Delta\Phi - E)$, where $\Delta\Phi$ is the tunneling energy window and E is the electron energy after tunneling to the conduction band (CB) side. Considering the conservation of transverse energy, the barrier seen by an electron at the classical turning point on the VB side is $E_g + (\Delta\Phi - (E_\parallel - 2E_\perp))$ [Fig. 2(b)], where $E_\parallel$ is the longitudinal electron energy after tunneling at the CB side and $E_\perp$ is the transverse energy, which is constant during tunneling. Therefore, the effective bandgap seen by a longitudinal k-state is given

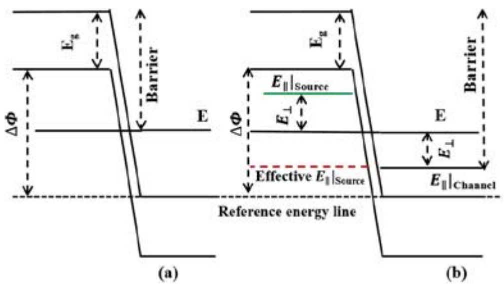

Fig. 2. (a) Schematic of band diagram showing the barrier in a pure 1-D tunneling case ($E_\perp = 0$). (b) Taking conservation of transverse energy the effective barrier and bandgap is modified as shown.

by [23], $E_g^* = E_g + 2E_\perp$, where $E_\perp = \hbar^2(k_x^2 + k_y^2)/2m^*$. Now, the transmission probability for a given transverse electron energy ($E_\perp$) state can be written as [24]

$$T(E_\perp) = \exp\left(-\frac{4\sqrt{2m^*}}{3q\hbar F} E_g^{*\frac{3}{2}}\right) \tag{1}$$

where F is the local electric field, which is taken to be constant, m^* is the reduced tunneling mass, and $E_g{}^*$ is the effective bandgap seen by the electron/hole while tunneling. The electric field is taken to be 2/3 times (considering an exponentially decaying potential profile [25]) of the peak junction field

$$F = \frac{2\left(E_g^* + \Delta\Phi\right)}{3q\Lambda} \tag{2}$$

where $\Delta\Phi$ is the tunneling window [Fig. 1(b)], which depends on the surface potential of the channel, and Λ is the screening length given by [25]

$$\Lambda = \sqrt{\frac{\epsilon_{\mathrm{InN}}}{\epsilon_{\mathrm{ox}}} t_{\mathrm{InN}} t_{\mathrm{ox}}}. \tag{3}$$

Substituting the effective barrier and tunnel screening length in (1), the expression for the transmission probability for a given $E_\perp$ is

$$T(E_\perp) = \exp\left(-\frac{2\Lambda\sqrt{2m^*}}{\hbar(E_g + 2E_\perp + \Delta\Phi)}(E_g + 2E_\perp)^{\frac{3}{2}}\right). \tag{4}$$

The total number of tunneling modes for a given longitudinal energy is obtained by summing over the allowed transverse energy states, $T(E_\|) = \sum_{E_\perp} T(E_\perp)$. $E_\perp$ can lie between 0 and $E_{\max}$, where $E_{\max} = \min(E_{\mathrm{vm}} - E_\|, E_\| - E_{\mathrm{cm}})$ $[E_\| = \hbar^2 k_z^2/2m^*]$. Here, E_{vm} and E_{cm} are the minima of VB on the source side and maxima of CB on the channel side, respectively. With this, the total number of tunneling modes for a given longitudinal energy is given by (summation can be converted to an integral [26] with the aid of 2-D density of states in energy space)

$$T(E_\|) = \int_0^{E_{\max}} \rho(E_\perp) T(E_\perp)\, dE_\perp \tag{5}$$

where $\rho(E_\perp)$ $(= \sqrt{m_e m_h}/\pi\hbar^2)$ is the 2-D density of states in energy space.

Fig. 3(a) shows the tunneling probability $T(E_\|)$ normalized by $\int_0^{E_{\max}} \rho(E_\perp) dE_\perp = \sqrt{m_e m_h}/\pi\hbar^2 \cdot E_{\max}$ as a function of

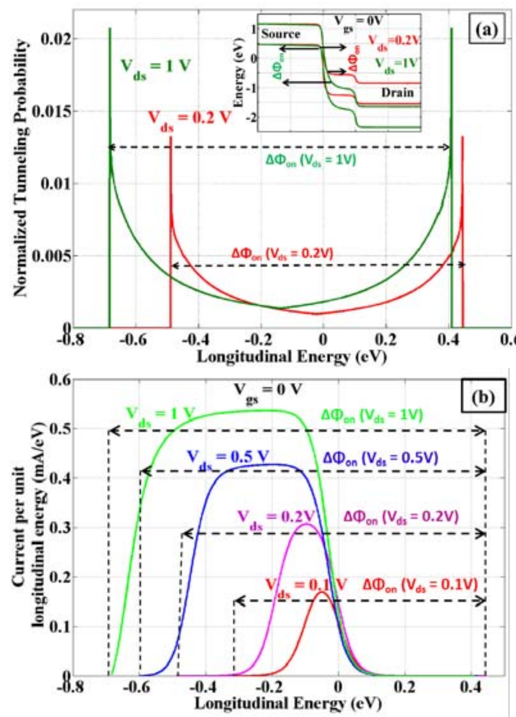

Fig. 3. (a) Tunneling probability as a function of longitudinal tunneling energy for $V_{\mathrm{gs}} = 0.2$ V and $V_{\mathrm{gs}} = 1$ V. Inset: simulated band diagram at $V_{\mathrm{gs}} = 0.2$ V and $V_{\mathrm{gs}} = 1$ V. (b) Normalized tunneling current as a function of longitudinal tunneling energy for increasing V_{ds}.

$E_\|$ for different applied V_{ds} and $V_{\mathrm{gs}} = 0$ V. As observed in the figure, when V_{ds} is increased the tunneling window ($\Delta\Phi$) increases, which increases the tunnel probability (4). As the longitudinal energy moves toward the edges of tunnel energy window ($\Delta\Phi$), number of tunneling modes per longitudinal state decreases but the normalized tunneling probability (ratio of tunneling modes to total modes) increases and finally drops to zero at the band edges.

Now, with the effective bandgap E_g^* and the transverse energy states taken care of within $T(E_\|)$, 1-D tunneling current is given by

$$J_{\mathrm{ds}} = \frac{2q}{h}\int_0^{\Delta\Phi} T(E_\|)(f_L(E_\|) - f_R(E_\|))dE_\| \tag{6}$$

where $f_L(E_\|)$ and $f_R(E_\|)$ are the Fermi distribution functions in the source and channel. The factor $2q/h$ is the quantum conductance for an electron. The total current is obtained from the dimensions of the device as $I = \iint J_{\mathrm{ds}} dA$. The tunneling current contributed by a longitudinal state $E_\|$ as a function of $E_\|$ is shown in Fig. 3(b). The tunneling current contribution for ($E_{\mathrm{FL}} < E < E_V$, E_{FL} is the hole quasi-Fermi level on the source side) is negligible due to the tail of the Fermi function ($f_L(E)$). The current again falls near the lower edge of the tunnel window ($\Delta\Phi$) on the CB side, as the tunnel probability reaches zero, as observed in Fig. 3(a).

B. DC Characteristics of InN TFET

Fig. 4(a) shows the semianalytically calculated and simulated I_{ds}–V_{gs} characteristics of the TFET. A good match

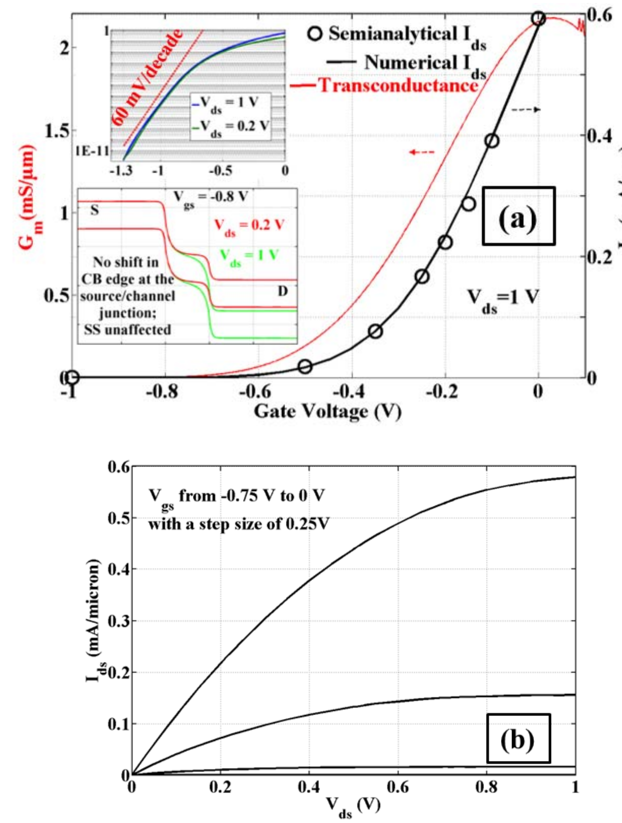

Fig. 4. (a) Input transfer characteristics of the InN TFET. Black and red solid lines: ATLAS simulated drain current and transconductance, respectively. Open circles: analytical drain current. Inset: SS below −1 V is less than 60 mV/decade. (b) Output characteristics obtained from ATLAS simulation.

is observed between the calculated and simulated currents verifying the model in the simulator. The ON ($V_{gs} = 0$ V)/OFF ($V_{gs} = -1$ V) current ratio of the device is 3.1×10^6 at $V_{ds} = 1.0$ V. The peak I_{ds} and G_m are 0.8 mA/μm and 2.18 mS/μm, respectively. The inset in Fig. 4(a) shows the SS of the device for two different drain biases. The SS is found to be around 44.2 mV/decade (for $I_{ds} \approx 10^{-11}$ mA/μm range), which is high due to large source doping [25]. It can be lowered using lower source doping but that would reduce G_m. The SS is found to be insensitive to drain bias. This is because tunnel energy window does not change with applied drain bias, as observed in the inset of Fig. 4(a). The simulated output characteristic of the device is shown in Fig. 4(b), which shows current saturation at higher V_{ds}. The current saturation occurs due to the formation of a barrier from drain to channel [Fig. 1(b)] at higher V_{ds} [25].

III. Avalanche Breakdown in the Channel

Next, we analyze the channel breakdown probability. As discussed in Section I, the gate-to-drain capacitance (C_{gd}) is a bottleneck for RF operations of TFETs, here we discuss the ways to reduce C_{gd} of TFETs. C_{gd} originates from the injection of electrons from drain to channel, which can be reduced if the barrier from drain to channel is increased. This can be achieved by increasing V_{ds}; however, increasing V_{ds} poses a risk of avalanche breakdown in the source/channel and drain-channel junctions. In the following section, we show

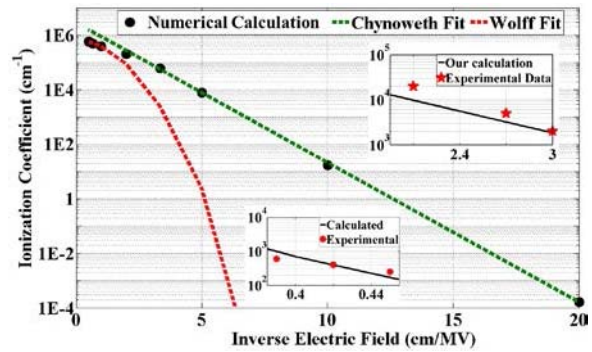

Fig. 5. Calculated electron ionization coefficient with electric field for InN. Inset: comparison of the calculation with experimental data for (top right) GaAs and (bottom left) GaN [30], [31]. Green and red lines: Chynoweth and Wolff fit to the calculated values.

from gate electrostatics and impact ionization calculations that avalanche breakdown is not likely even at $V_{ds} = 1.0$ V.

The avalanche breakdown in a junction is characterized by the ionization coefficient (α) and the junction breaks down if $\int_0^w \alpha dx > 1$ [24], where w is the width of the depletion region. Here, we show that InN TFET device can safely operate even at $V_{ds} = 1$ V without breaking down leading to a drastic reduction in C_{gd} and a significant increase in g_m as required for high frequency performance.

A. Calculation of Impact Ionization Coefficient (α) for InN

When electrons traverse through the high field region in the channel, they can undergo collision with the lattice and can emit or absorb phonons. Due to the high longitudinal optical (LO) ($E_R = 73$ meV [27]) phonon energy in InN, there are too few LO phonons present at room temperature to be absorbed by electrons. Therefore, electrons gain energy faster than energy loss by phonon emission. If the energy of an electron becomes equal to that of ionization energy then the electron can cause impact ionization producing electron-hole pair. The probability of impact ionization is characterized by the ionization coefficient (α), average number of impact ionization per unit length.

Here, we calculate the impact ionization coefficient in InN by solving the integral form of BTE following Baraff's method [28]. We included POP scattering in our calculation in addition to the mechanisms considered in [28]. Solving the integral form of BTE gives the nonequilibrium distribution function of electrons under high electric fields. The product of this function and the relative cross section of impact ionization gives the density of impact ionization. From which we can find out the impact ionization coefficient, which is the number of electrons causing impact ionization per unit length. The relative impact ionization cross section is calculated considering ionized impurity, acoustic deformation potential, optical deformation potential, and POP scatterings. We assumed a parabolic E-k dispersion and a constant mean free path, calculated to be 10 nm using a lucky drift model [29]. Fig. 5 shows the dependence of the calculated α in InN on the electric field. The insets in Fig. 5 show that similar calculations done for GaN and GaAs match well with the experimental data [30], [31]. The calculated impact ionization coefficient can

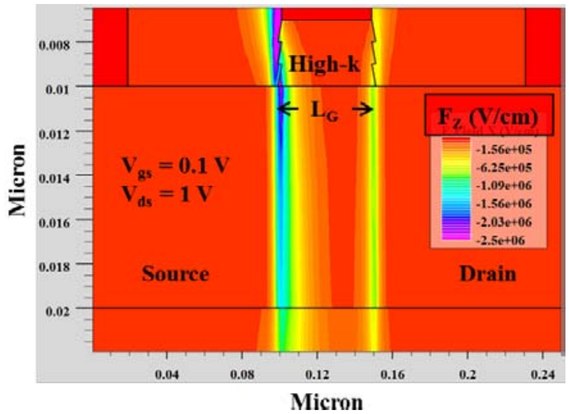

Fig. 6. 2-D longitudinal field (F_z) distribution in the source–channel junction in ON state ($V_{gs} = 0$ V and $V_{ds} = 1$ V) of the device.

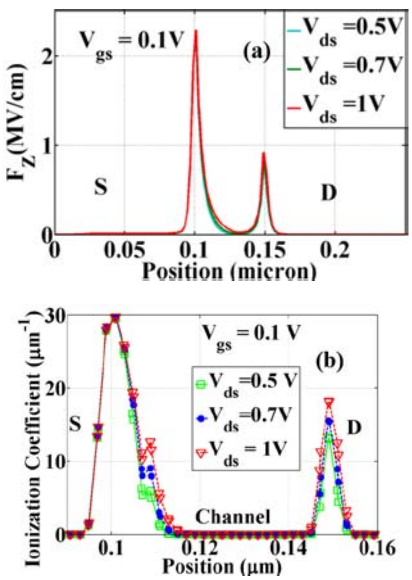

Fig. 7. (a) Variation of the longitudinal electric field across the channel. (b) Calculated ionization coefficient in the channel. It is estimated horizontal (Z) slice wise without considering any impact ionization interaction in the vertical (Y) direction.

TABLE III

$\int_0^w \alpha dx$ FOR DIFFERENT DRAIN BIASES

V_{ds} (V)	$\int_0^w \alpha dx\vert_{InN}$
0.1	0.5182
0.2	0.5573
0.5	0.6007
0.7	0.6754
1.0	0.7684

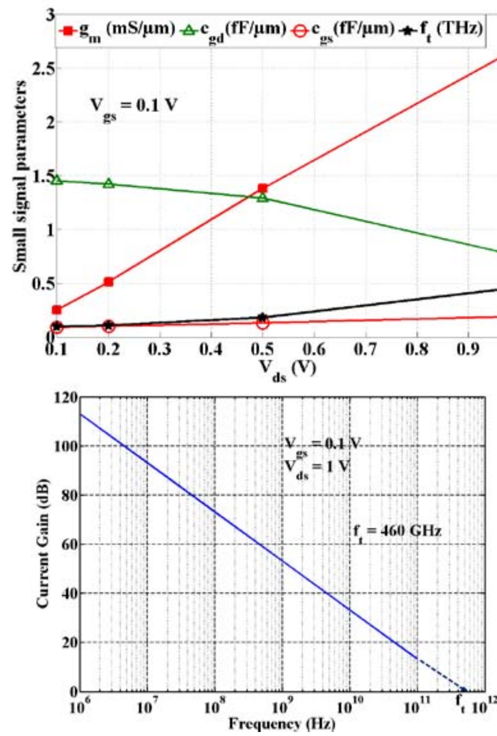

Fig. 8. (a) g_m, f_t, C_{gs}, and C_{gd} extracted from the small-signal simulation as a function of drain bias. (b) Short-circuit current gain for InN TFET at $V_{gs} = 0.1$ V and $V_{ds} = 1.0$ V.

be fitted in Chynoweth exponential form [$\alpha = a\exp(-b/F)$] [32] with $a = 2.9 \times 10^6$/cm and $b = 1.18$ MV/cm for ($1/F > 2$ cm/MV). In the high field region ($1/F < 2$ cm/MV), Wolff's fit [$\alpha = c\exp(-d/F^2)$] [33] is used with $c = 6.53 \times 10^5$/cm and $d = 0.5$ MV^2/cm^2.

B. Ionization Integral ($\int_0^w \alpha dx$) in the TFET Channel

2-D distribution of the longitudinal electric field (F_z) in the device is shown Fig. 6. Fig. 7(a) shows the longitudinal electric field in the channel at distance of 0.5 nm from the interface for increasing V_{ds}. Fig. 7(b) shows the ionization coefficient calculated using the Chynoweth and Wolff fit equations derived in the previous section. The calculated ionization integral is shown in Table III. As observed in the figure, the depletion region and peak electric field in the source/channel and channel/drain junctions increase with higher V_{ds}. However, the impact ionization coefficient rises slowly in the high field regions. Thus, it can be observed (Table III) that the value of the ionization integral does rise slowly with V_{ds}, but it remains below one even at $V_{ds} = 1.0$ V. It is observed that the ionization integral reaches 1.03 at a $V_{ds} = 2$ V. The large bandgap and optical phonon energy of InN make InN TFETs robust against ON state avalanche breakdown phenomenon.

IV. SMALL SIGNAL SIMULATION

Having established the safe operation at higher V_{ds}, we simulate the small signal performance under different V_{ds}. The calculated C_{gd} and C_{gs} from the simulated y-parameters and simulated f_t are plotted in Fig. 8(a) for increasing V_{ds}. At lower V_{ds}, extracted f_t is low ($f_t = 97$ GHz and $V_{ds} = 0.1$ V) due to the large C_{gd} as expected from TFET operation. However, as discussed before, C_{gd} is found to decrease [Fig. 8(a)] with increasing drain bias due to higher drain to channel barrier. The C_{gs} [Fig. 8(a)] remains almost unchanged with drain bias. In addition, the transconductance (g_m) of the device increases with drain bias. Significant increase in current and transconductance occurs because of the simultaneous effect of tunneling probability increase and a reduction of electrons with negative k_z states (due to higher drain to channel barrier) in the channel at higher V_{ds}. The decreasing C_{gd} and increasing g_m together boost up f_t. The device gives a peak current gain cutoff frequency of 460 GHz [Fig. 8(b)] at 1 V drain bias. Further scaling of the device can achieve terahertz cutoff frequencies.

V. Conclusion

In summary, we investigated the high frequency performance of InN TFET. It has been shown that a relatively low gate-to-drain capacitance (C_{gd}) and hence a higher f_t can be achieved at higher drain bias ($V_{ds} = 1$ V). It has also been quantitatively shown that the device does not undergo avalanche breakdown at high drain bias. The relation between the ionization coefficient and electric field for InN devices is also explored, which can be useful in future for development of other InN devices as well.

References

[1] K. Bernstein, R. K. Cavin, W. Porod, A. Seabaugh, and J. Welser, "Device and architecture outlook for beyond CMOS switches," *Proc. IEEE*, vol. 98, no. 12, pp. 2169–2184, Dec. 2010.

[2] A. C. Seabaugh and Z. Qin, "Low-voltage tunnel transistors for beyond CMOS logic," *Proc. IEEE*, vol. 98, no. 12, pp. 2095–2110, Dec. 2010.

[3] S. Cho, J. S. Lee, K. R. Kim, B. G. Park, J. S. Harris, and I. M. Kang, "Analyses on small-signal parameters and radio-frequency modeling of gate-all-around tunneling field-effect transistors," *IEEE Trans. Electron Devices*, vol. 58, no. 12, pp. 4164–4171, Dec. 2011.

[4] S. Mookerjea, R. Krishnan, S. Datta, and V. Narayanan, "On enhanced Miller capacitance effect in interband tunnel transistors," *IEEE Electron Device Lett.*, vol. 30, no. 10, pp. 1102–1104, Oct. 2009.

[5] S. O. Koswatta, M. S. Lundstrom, and D. E. Nikonov, "Performance comparison between p-i-n tunneling transistors and conventional MOSFETs," *IEEE Trans. Electron Devices*, vol. 56, no. 3, pp. 456–465, Mar. 2009.

[6] S. O. Koswatta, S. J. Koester, and W. Haensch, "On the possibility of obtaining MOSFET-like performance and sub-60-mV/dec swing in 1-D broken-gap tunnel transistors," *IEEE Trans. Electron Devices*, vol. 57, no. 12, pp. 3222–3230, Dec. 2010.

[7] K. Boucart and A. M. Ionescu, "Double-gate tunnel FET with high-k gate dielectric," *IEEE Trans. Electron Devices*, vol. 54, no. 7, pp. 1725–1733, Jul. 2007.

[8] D. Mohata *et al.*, "Experimental staggered-source and N^+ pocket-doped channel III-V tunnel field-effect transistors and their scalabilities," *Appl. Phys. Exp*, vol. 4, no. 2, p. 024105, Feb. 2011.

[9] K. Ganapathi, Y. Yoon, and S. Salahuddin, "Analysis of InAs vertical and lateral band-to-band tunneling transistors: Leveraging vertical tunneling for improved performance," *Appl. Phys. Lett.*, vol. 97, no. 3, p. 033504, Jul. 2010.

[10] R. Bijesh *et al*, "Demonstration of InGaAs/GaAsSb near broken-gap tunnel FET with $I_{ON} = 740\ \mu A/\mu m$, $G_m = 700\ \mu S/\mu m$ and gigahertz switching performance at $V_{DS} = 0.5$ V," in *Proc. IEEE Int. Electron Devices Meeting (IEDM)*, Dec. 2013, pp. 28.2.1–28.2.4.

[11] *ATLAS Device Simulation Software*, Silvaco Inc, Santa Clara, CA, USA, Mar. 2014.

[12] K. T. Tsen, C. Poweleit, D. K. Ferry, H. Lu, and W. J. Schaff, "Observation of large electron drift velocities in InN by ultrafast Raman spectroscopy," *Appl. Phys. Lett.*, vol. 86, no. 22, pp. 222103-1–222103-3, May 2005.

[13] S. K. O'Leary, B. E. Foutz, M. S. Shur, and L. F. Eastman, "Steady-state and transient electron transport within bulk wurtzite indium nitride: An updated semiclassical three-valley Monte Carlo simulation analysis," *Appl. Phys. Lett.*, vol. 87, no. 22, p. 222103, Nov. 2005.

[14] S. K. O'Leary, B. E. Foutz, M. S. Shur, and L. F. Eastman, "Potential performance of indium-nitride-based devices," *Appl. Phys. Lett.*, vol. 88, no. 15, p. 152113, Apr. 2006.

[15] Y.-S. Lin, S.-H. Koa, C.-Y. Chan, S. S. H. Hsu, H.-M. Lee, and S. Gwo, "High current density In*N*/Al*N* heterojunction field-effect transistor with a SiN_x gate dielectric layer," *Appl. Phys. Lett.*, vol. 90, no. 14, p. 142111, Apr. 2007.

[16] P. D. C. King, T. D. Veal, and C. F. McConville, "Unintentional conductivity of indium nitride: Transport modelling and microscopic origins," *J. Phys., Condens. Matter*, vol. 21, no. 17, p. 174201, Apr. 2009.

[17] D. Segev and C. G. Van de Walle, "Origins of Fermi-level pinning on GaN and InN polar and nonpolar surfaces," *Europhys. Lett.*, vol. 76, no. 2, p. 305, Sep. 2006.

[18] S. Choi, F. Wu, O. Bierwagen, and J. S. Speck, "Polarity control and transport properties of Mg-doped (0001) InN by plasma-assisted molecular beam epitaxy," *J. Vac. Sci. Technol. A*, vol. 31, no. 3, p. 031504, Mar. 2013.

[19] J. Simon, V. Protasenko, C. Lian, H. Xing, and D. Jena, "Polarization-induced hole doping in wide-band-gap uniaxial semiconductor heterostructures," *Science*, vol. 327, no. 5961, pp. 60–64, Jan. 2010.

[20] J. Simon *et al.*, "Polarization-induced zener tunnel junctions in wide-band-gap heterostructures," *Phys. Rev. Lett.*, vol. 103, no. 2, p. 026801, Jul. 2009.

[21] C. T. Kuo *et al.*, "Is electron accumulation universal at InN polar surfaces?" *Appl. Phys. Lett.*, vol. 98, no. 5, pp. 052101–052103, Jan. 2011.

[22] C.-L. Wu, H.-M. Lee, C.-T. Kuo, C.-H. Chen, and S. Gwo, "Absence of Fermi-level pinning at cleaved nonpolar InN surfaces," *Phys. Rev. Lett.*, vol. 101, no. 10, p. 106803, Sep. 2008.

[23] C. Sandow, J. Knoch, C. Urban, Q.-T. Zhao, and S. Mantl, "Impact of electrostatics and doping concentration on the performance of silicon tunnel field-effect transistors," *Solid-State Electron.*, vol. 53, no. 10, pp. 1126–1129, Oct. 2009.

[24] S. M. Sze, "Tunnel diode and backward diode and p-n junction diodes," in *Physics of Semiconductor Devices*. New York, NY, USA: Wiley, 1969

[25] B. Rajamohanan, D. Mohata, A. Ali, and S. Datta, "Insight into the output characteristics of III-V tunneling field effect transistors," *Appl. Phys. Lett.*, vol. 102, no. 9, pp. 092105-1–092105-5, Mar. 2013.

[26] M. Lundstrom, "The quantum foundation," in *Fundamentals of Carrier Transport*. Cambridge, U.K.: Cambridge Univ. Press, 2000.

[27] N. A. Masyukov and A. V. Dmitriev, "Hot electrons in wurtzite indium nitride," *J. Appl. Phys.*, vol. 109, no. 2, pp. 023706-1–023706-6, Jan. 2011.

[28] G. A. Baraff, "Distribution functions and ionization rates for hot electrons in semiconductors," *Phys. Rev.*, vol. 128, no. 6, pp. 2507–2517, Dec. 1962.

[29] E. Bringuier, "High-field transport statistics and impact excitation in semiconductors," *Phys. Rev. B*, vol. 49, no. 12, p. 7974, Mar. 1994.

[30] H. Shichijo and K. Hess, "Band-structure-dependent transport and impact ionization in GaAs," *Phys. Rev. B*, vol. 23, no. 8, p. 4197, Apr. 1981.

[31] B. J. Baliga, "Gallium nitride devices for power electronic applications," *Semicond. Sci. Technol.*, vol. 28, no. 7, p. 074011, Jun. 2013.

[32] A. G. Chynoweth, "Ionization rates for electrons and holes in silicon," *Phys. Rev.*, vol. 109, no. 5, p. 1537, Mar. 1958.

[33] P. A. Wolff, "Theory of electron multiplication in silicon and germanium," *Phys. Rev.*, vol. 95, no. 6, p. 1415, Sep. 1954.

Krishnendu Ghosh (S'11) received B.E. degree from Bengal Engineering and Science University, Shibpur, India in 2012. He is currently pursuing his MS degree in Electrical Engineering at the University at Buffalo, The State University of New York. His research interests include carrier transport in nanoscale, avalanching in semiconductors and modelling of novel devices like fin-FETs, tunnel-FETs.

Uttam Singisetti (S'02–M'09) received the B.Tech. degree from IIT Madras, Chennai, India, in 2001, the M.S. degree from Arizona State University, Tempe, AZ, USA, in 2004, and the Ph.D. degree in electrical engineering from the University of California at Santa Barbara, Santa Barbara, CA, USA, in 2009.

He is currently an Assistant Professor with the University at Buffalo, The State University of New York, Buffalo, NY, USA.